Pressure and temperature dependence of shock remanence intensity for single-domain titanomagnetite-bearing basalt: Toward understanding the magnetic anomalies produced by impact events

Masahiko Sato[1]*, Kosuke Kurosawa[2], Sunao Hasegawa[3], and Futoshi Takahashi[4]

[1]Department of Earth and Planetary Science, The University of Tokyo, Tokyo, Japan

[2]Planetary Exploration Research Center, Chiba Institute of Technology, Narashino, Japan

[3]Institute of Space and Astronautical Science, Japan Aerospace Exploration Agency, Sagamihara, Japan

[4]Department of Earth and Planetary Sciences, Kyushu University, Fukuoka, Japan

*Department of Earth and Planetary Science, The University of Tokyo, 7-3-1 Hongo, Bunkyo-ku, Tokyo 113-0033 Japan

Key points

- Two series of shock remanence acquisition and evaluation experiments are conducted by varying applied field and impact conditions.

- An empirical expression for shock remanence intensity is proposed to be the power function of pressure and a linear function of temperature.

- The magnetic anomaly over an impact crater estimated from the empirical equation shows a distinct pattern approximated as two dipoles.

Abstract

Knowledge of shock remanent magnetization (SRM) property is crucial for interpreting the spatial change in a magnetic anomaly observed over an impact crater. This study conducted two series of impact-induced SRM acquisition experiments by varying the applied field and impact conditions, and the remanences of cube-shaped subsamples cut from shocked basalt containing single-domain titanomagnetite were measured to

investigate the pressure and temperature dependence of the SRM intensity. The peak pressure and peak temperature distributions in the shocked samples were estimated using shock-physics modeling. SRM intensity was proportional to the apple field intensity up to 400 μT. The SRM intensities under different projectile conditions were consistent at the same pressure values. An empirical equation of SRM intensity is proposed to be the power function of pressure and a linear function of temperature, which can express the experimental SRM intensity values in a range of pressures up to 10 GPa and temperatures up to the Curie temperature. The magnetic anomaly estimation over an impact crater was demonstrated using the empirical equation, and the anomaly distribution shows a distinct feature approximated as a combination of two dipoles located at the basement of the crater and a deeper part.

Plain Language Summary

Knowledge of shock remanence is crucial for interpreting the spatial change in a magnetic anomaly observed over an impact crater and for reconstructing the magnetic field histories of terrestrial planets. This study conducted a suite of shock remanence

49 acquisition and evaluation experiments to investigate the pressure and temperature
50 dependence of shock remanence intensity. An empirical expression of shock remanence
51 intensity is proposed on the basis of experimental data, and the magnetic anomaly
52 estimation is demonstrated using the proposed empirical equation. The anomaly shows a
53 distinct feature approximated as a combination of two dipoles located at the basement of
54 the crater and a deeper part, and the feature could be used to detect the magnetic anomaly
55 caused by impact events.
56
57 **1. Introduction**
58 Magnetic anomaly records caused by past impact events play an important role
59 in reconstructing the magnetic field histories of terrestrial planets (Acuña et al., 1999;
60 Halekas et al., 2003; Lillis et al., 2013). At the time of impact events, crustal rocks in
61 terrestrial planets can record shock remanent magnetization (SRM) as a result of shock
62 wave propagation. Knowledge of the spatial distribution of SRM intensity is crucial for
63 interpreting the magnetic anomaly over the impact craters and for reconstructing the
64 paleo-planetary field intensity based on the magnetic field datasets from present

observations and future explorations. Nevertheless, the SRM intensity distribution is poorly understood because of the difficulty in evaluating the magnetization distribution within the experimentally SRM-imparted samples. Although post-impact remanence modifications, such as thermoremanent magnetization (TRM) acquisition of a melt sheet (Hood, 2011) and chemical remanent magnetization acquisition due to hydrothermalism (Quesnel et al., 2013), are also important for interpreting crustal remanence distributions, the initial structure of remanent magnetization immediately after the impacts should be explored.

Srnka et al. (1979) qualitatively demonstrated that the SRM intensities decreased with increasing distance from the impact point for multidomain (MD) titanomagnetite-bearing basalt using core samples drilled from a shocked basalt plate. Gattacceca et al. (2008) conducted laser-induced SRM acquisition experiments and remanence measurements of subsamples for pseudo-single-domain (PSD) titanomagnetite-bearing basalt and MD magnetite-bearing microdiorite. The SRM intensities were homogeneous in their experimental samples (Gattacceca et al., 2008), which was further supported by superconducting quantum interference device

81 microscopy measurements for the SRM-bearing basalt (Gattacceca et al., 2010). Sato et
82 al. (2021) established the SRM acquisition method using a two-stage light gas gun and
83 the remanence evaluation method for divided subsamples, and systematic spatial changes
84 in SRM intensity and stability were observed for a single-domain (SD) titanomagnetite-
85 bearing basalt cylinder. Although the spatial changes in SRM intensities were
86 qualitatively evaluated and were different for each magnetic mineral in these previous
87 studies, the quantitative evaluation of SRM intensity with respect to the shock wave
88 conditions such as pressure and temperature changes has not yet been obtained, and
89 further investigation is required to quantitatively understand the relationship between the
90 magnetic anomaly observation data and the crustal remanence originating from the
91 impact event.

92 Using a magnetically well-characterized basalt sample bearing fine-grained SD
93 titanomagnetite, the SRM acquisition experiments, remanence measurements for cube-
94 shaped subsamples cut from the SRM-imparted samples, and impact simulations were
95 conducted for quantitatively investigating the pressure and temperature dependence of
96 SRM intensity. In one series of experiments, impact experiments were conducted under

97 magnetic fields of 100–400 μT at a nearly constant impact velocity, whereas in the other
98 series of experiments, the impact velocities were set to 1.3–7.0 km/s with different
99 projectiles and a constant applied field value. The peak pressure and peak temperature
100 distributions after the impacts were estimated using shock-physics modeling. Based on
101 the results of the remanence measurements and modeling, we propose an empirical
102 relationship between the SRM intensity and peak pressure/temperature in impact events.
103 In addition, we calculated the magnetic anomaly profile over an impact crater using the
104 empirical equation.
105
106 **2. Method**
107 A natural basalt sample (Linxi, Inner Mongolia) was used for the experiments.
108 The basalt samples were the same as those used for the SRM experiments in the study by
109 Sato et al. (2021), and the detailed rock magnetic properties have been reported in a
110 previous study. The basalt sample contained SD titanomagnetite with a Curie temperature
111 of 237ºC (Sato et al., 2021). Cylindrical basalt samples with a diameter and length of 8
112 cm were used as targets in the SRM acquisition experiments. The cylindrical basalt

113 samples were subjected to a three-axial alternating field demagnetization (AFD) of 80
114 mT using a DEM-8601C AF demagnetizer (Natsuhara-Giken) before the SRM
115 acquisition experiments.

116 Two-stage light-gas guns (vertical and horizontal) at the Institute of Space and
117 Astronautical Science (ISAS) of the Japan Aerospace and Exploration Agency (JAXA)
118 were used for SRM acquisition experiments. This study follows the method employed by
119 Sato et al. (2021). The basalt cylinder, solenoid coil, and magnetic shield were placed
120 coaxially in a vacuum experimental chamber. An aluminum sphere with a diameter of 2
121 mm and a polycarbonate sphere with a diameter of 7 mm were used as the projectiles,
122 and a nylon slit sabot was used to accelerate the projectile (Kawai et al., 2010). The impact
123 angle was fixed at 90°, measured from the top flat surface of the basalt cylinder, that is,
124 vertical impacts. Two series of experiments were conducted (Table 1). In one series of
125 experiments, impact experiments were conducted under magnetic fields of 100, 150, 200,
126 and 400 μT with nearly constant impact velocities of 5.3–5.5 km/s. In the other series of
127 experiments, the magnetic field was fixed at 100 μT, and the impact velocities were set
128 to 1.3 (polycarbonate), 2.7, 4.0, 5.3, and 7.0 km/s (aluminum).

129 After the impact experiments on SRM acquisition, the target samples were cut
130 into cube-shaped subsamples approximately 3 mm in length using rock cutters. The
131 subsamples are denoted as *R*i*Z*j, where the indices i and j are the numbers from the impact
132 point in the radial and axial directions of a cylindrical sample. The measured subsamples
133 are listed in Table 2. Remanence measurements were conducted using a superconducting
134 quantum interference device magnetometer (Model 755, 2G Enterprise) at the University
135 of Tokyo. This study followed the method of Sato et al. (2015) for small-sample
136 measurements. The cube-shaped subsample was set at the edge of a rod made of polylactic
137 acid using a double-sided tape. The remanence of the polylactic acid rod was measured
138 before and after sample measurement, and the average remanence of the rod was
139 subtracted to calculate the sample moment. Stepwise AFD treatments of up to 80 mT were
140 conducted using an alternating field demagnetizer (DEM-95C, Natsuhara-Giken) with a
141 two-axis tumbling system. After the stepwise AFD measurements of the SRM state,
142 several samples were selected for each cylindrical sample, and the anhysteretic remanent
143 magnetization (ARM) with DC and AC fields of 100 μT and 80 mT, respectively, were
144 measured to normalize the effect of heterogeneity of magnetic minerals. Additionally,

145 stepwise thermal demagnetization (THD) treatments up to 320°C were conducted on eight
146 cube samples selected from one cylindrical basalt sample using a thermal demagnetizer
147 (TDS-1, Natsuhara-Giken).

148 A series of impact simulations using a two-dimensional version of the iSALE
149 shock physics code (Amsden et al., 1980; Ivanov et al., 1997; Wünnemann et al., 2006)
150 was conducted to estimate the peak pressure P_{peak} and peak temperature T_{peak} values in
151 the SRM acquisition experiments. This study followed the impact simulations of Sato et
152 al. (2021), and the details of the impact simulation are described in their paper. The impact
153 velocities and shapes of the projectile and target in the simulation were set to the same
154 values as those in the SRM acquisition experiments. The mass-weighted averaged values
155 of P_{peak} and T_{peak} in each 3 mm cube region were calculated to compare the calculated
156 peak pressures and peak temperatures with the experimentally measured SRM properties.
157

158 **3. Results**

159 The experimental results for an aluminum sphere with a diameter of 2 mm and
160 an impact velocity of 7 km/s (cylindrical basalt samples 3767 and 3769) are summarized

161 in Figures 1–3. The SRM component was calculated as $\boldsymbol{J}_{SRM}(2) - \boldsymbol{J}_{SRM}(80)$ and the
162 stability of the SRM component was evaluated as $|\boldsymbol{J}_{SRM}(6) - \boldsymbol{J}_{SRM}(80)|/|\boldsymbol{J}_{SRM}(2) -$
163 $\boldsymbol{J}_{SRM}(80)|$, where $\boldsymbol{J}_{SRM}(X)$ is the SRM vector at the X mT AFD step. The basalt sample
164 acquired SRM and the SRM properties were systematically change with increasing the
165 distance from impact point as observed in Sato et al. (2021): (1) The SRM component is
166 a single component in one direction in the orthogonal vector plots (Figure 1). (2) The
167 SRM intensity systematically changes with distance in the case with an applied field of
168 100 μT, and the SRM intensity in the case with an applied field of 100 μT is larger than
169 that of the zero field (Figure 2), indicating that the basalt sample acquired remanent
170 magnetization as a result of shock wave propagation in the applied magnetic field. (3)
171 The SRM intensity systematically changed with distance from the impact point (Figure
172 2). (4) The SRM stability with respect to the AFD treatment systematically changed with
173 distance from the impact point, and the median destructive field of the SRM components
174 was less than 20 mT (Figure 3).
175 The experimental results for cylindrical basalt samples with different sizes and
176 the same projectile condition (aluminum sphere with a diameter of 2 mm and impact

177 velocity of approximately 7 km/s) are compared in Figure 4. The diameters and lengths
178 of the basalt samples were 8 cm (this study) and 10 cm (Sato et al., 2021), respectively.
179 To normalize the heterogeneity of magnetic minerals among the cylindrical basalt
180 samples, the SRM intensity was normalized as $|\boldsymbol{J}_{\mathrm{SRM}}(2) - \boldsymbol{J}_{\mathrm{SRM}}(80)|/J_{\mathrm{ARM}}$, where J_{ARM} is
181 the average ARM intensity for several cube samples. The 10 cm basalt cylinder sample
182 shows a systematic change in the normalized SRM intensity with approximately 0.1
183 dispersion at the same P_{peak} value. The changes in the normalized SRM intensity with
184 respect to P_{peak} for the 8 cm basalt cylinder were consistent with those of the 10 cm basalt
185 cylinder within 3–4 cm from the impact point, while the SRM intensity for the 8 cm
186 cylinder deviated from the trend for the 10 cm cylinder beyond 3–4 cm from the impact
187 point. This deviation likely arose from the arrival of an expansion wave from the side of
188 the cylinder, where a free surface exists. Although the effects of sudden pressure release
189 due to the expansion wave from the side surface are not yet fully understood, the geometry
190 is largely different from that of natural impact events. Consequently, we decided to use
191 only the SRM data within 3 cm from the impact point where the pressure release occurred
192 because of the expansion wave from the top surface.

193 The results of the stepwise THD treatments in the case of an aluminum sphere
194 with a diameter of 2 mm and an impact velocity of 5.3 km/s (cylindrical basalt sample
195 835) are summarized in Figures 5 and 6. The SRM component was a single component
196 in one direction in the orthogonal vector plot (Figure 5), similar to the stepwise AFD
197 treatments (Figure 1). In contrast to the AFD treatment, the SRM stability with respect to
198 the THD treatment was almost unchanged with the distance from the impact point (Figure
199 6).

200 The experimental results in the case of an aluminum sphere with a diameter of
201 2 mm and nearly-identical impact velocity (5.3–5.5 km/s) and varying the applied field
202 intensity (cylindrical basalt samples 835, 838, 839, and 840) are shown in Figures 7a and
203 7b. The SRM intensity was normalized as $\{|\boldsymbol{J}_{SRM}(2) - \boldsymbol{J}_{SRM}(80)|/B_{SRM}\}/(J_{ARM}/B_{ARM})$,
204 where B_{SRM} and B_{ARM} are the applied DC field intensities for the SRM and ARM,
205 respectively. The normalized SRM intensities and SRM stabilities at 150, 200, and 400
206 μT showed similar values over the entire pressure range. The normalized SRM intensity
207 and SRM stability values in the cases of 100 μT slightly deviated from the trends of higher
208 field intensities below ~0.5 and ~1 GPa, respectively. These deviations increased with

209 decreasing pressure. These deviations indicate that the SRM properties below ~1 GPa
210 were saturated above 100 μT field conditions. Despite slight saturation, the normalized
211 SRM intensity and SRM stability values were similar in the four cylindrical samples
212 (Figure 7b); thus, the SRM intensity was proportional to the applied field intensity up to
213 400 μT.

214 The experimental results for an applied field intensity of 100 μT and various
215 projectile conditions (cylindrical basalt samples 835, 836, 837, 3767, and 3773) are
216 shown in Figures 7c and 7d. The SRM intensity increased with increasing P_{peak} value and
217 deviated from the increasing trend near the impact point owing to the significant
218 temperature increase for each cylindrical sample (Figure 7c). The deviation from this
219 trend becomes significant above 310 K (Figure 8). Comparing the regions with the
220 increasing trend, the SRM intensities for the different projectile conditions were almost
221 consistent at the same P_{peak} values, although the SRM intensities of the slowest aluminum
222 projectile velocity samples were slightly higher than those of the other samples (Figure
223 7c). The SRM stability systematically increased with increasing P_{peak} value, even in the
224 case T_{peak} values above 310 K, and all basalt cylinder samples showed a consistent trend

225 (Figure 7d).

226

227 **4. Discussion**

228 The SRM intensity approximated as linear and power functions of the P_{peak}
229 value for cube samples with T_{peak} below 310 K are shown in Figure 7c. The difference
230 between the linear regression line and experimental data was significant below 0.2 GPa,
231 while the experimental data agreed well with the power function for the entire P_{peak} range
232 (Figure 7c). The SRM intensity dependence on T_{peak} value is assumed to be a linear
233 function because the T_{peak} variations in the experimental data are sparse compared to the
234 P_{peak} variations. The root mean square of the differences between the estimated value and
235 the experimental value were 0.065 and 0.043 for linear and power functions of the P_{peak},
236 respectively. Thus, this study proposes a power function as an empirical expression for
237 the SRM intensity dependence on P_{peak} value, and the SRM intensity J_{SRM} was
238 approximated for the entire P_{peak} and T_{peak} ranges as

239 $$\frac{J_{\mathrm{SRM}}}{J_{\mathrm{ARM}}} = 7.09 \times 10^{-1} \times \left(\frac{P_{\mathrm{peak}}}{\mathrm{GPa}}\right)^{0.134} - 1.19 \times 10^{-3} \left(\frac{T_{\mathrm{peak}}}{\mathrm{K}}\right) \quad (1).$$

240 The experimental and modeled SRM intensities are compared in Figure 9. The intensity

241 differences between the experimental and model values were smaller than the SRM
242 intensity values over the entire P_{peak} and T_{peak} ranges.

243 The efficiencies of TRM and ARM acquisition for the basalt sample were 46.0
244 and 12.0 $Am^2kg^{-1}T^{-1}$, respectively, and the SRM acquisition efficiency with respect to
245 TRM is expressed as

246 $$\frac{J_{SRM}}{J_{TRM}} = 1.85 \times 10^{-1} \times \left(\frac{P_{peak}}{GPa}\right)^{0.134} - 3.10 \times 10^{-4} \left(\frac{T_{peak}}{K}\right) \quad (2),$$

247 where J_{TRM} is the TRM intensity. Additionally, the law of proportionality of the
248 remanence intensity to the applied field intensity was almost satisfied for the SRM in this
249 study. Then, the empirical SRM intensity relationship with respect to the applied field
250 intensities B, P_{peak}, and T_{peak} is given as

251 $$J_{SRM} = \left\{1.85 \times 10^{-1} \times \left(\frac{P_{peak}}{GPa}\right)^{0.134} - 3.10 \times 10^{-4} \left(\frac{T_{peak}}{K}\right)\right\} \times J_{TRM}(B_0) \times \frac{B}{B_0} \quad (3),$$

252 where $J_{TRM}(B_0)$ is the TRM intensity at the acquisition field of B_0.

253 Based on the empirical equation, we estimated the magnetic anomaly profile
254 over an impact crater on basaltic crust containing SD titanomagnetite. Given that the SD
255 titanomagnetite grains contained in the basaltic crust are identical to those in our
256 experimental sample, the empirical equation for SRM acquisition can be applied to the

257 basaltic crust. The P_{peak} and T_{peak} distributions in the basaltic crust were calculated using
258 the iSALE shock-physics code (Figures 10c and 10d). Details of the shock physics
259 modeling are provided in the Supporting Information. The P_{peak} and T_{peak} values were
260 substituted into the empirical equation (2), and the crustal remanence intensity with
261 respect to the TRM intensity was calculated for the basaltic crust. The crustal rock near
262 the impact point experiences a high temperature during and after the shock wave
263 propagation and should acquire TRM. Then, the TRM values were allocated to the crustal
264 rocks with T_{peak} values above the Curie temperature of titanomagnetite (510 K). The
265 magnetic field was vertically applied to the basaltic crust, and the crustal rock acquired
266 TRM and SRM parallel to the applied field. Because our empirical relationship cannot
267 evaluate the effects of lithostatic pressure and geotherm, zero pressure and uniform
268 temperature in the basaltic crust were assumed to be the initial conditions, which
269 correspond to the craters produced on a laboratory scale. Nevertheless, our simulation
270 may provide a qualitative understanding of the magnetic anomaly profile above the
271 magnetized crater immediately after impact.

272 The distribution of the crustal remanence is illustrated in Figure 10b. A thin

273 layer of approximately one projectile radius (R_p) around the impact point acquired a
274 strong remanence as TRM, and a vast region outside the TRM layer (20–30 R_p) acquired
275 a significant SRM intensity (>0.05 J_{TRM}). Consequently, the magnetic anomaly at an
276 altitude comparable to the crater diameter (20 R_p) showed a broader distribution with
277 respect to the crater shape (Figure 10a). The contributions of the TRM and SRM regions
278 to the magnetic anomaly are evaluated in Figure 10a. The contribution of the SRM region
279 is three times higher than that of the TRM layer at the center of the crater. These
280 contributions can be approximated as dipole moments located at depths of 10 R_p and 43
281 R_p for the TRM and SRM regions, respectively. The intensity of latter dipole is ten times
282 larger than that of former. The depth of 43 R_p corresponds to the P_{peak} value of
283 approximately 0.1 GPa and the SRM intensity of 0.04–0.05 J_{TRM}. The remanence
284 intesnsity decreases with increasing the distance from the impact point in the SRM region,
285 and the volume of the same distance area increases with increasing the distance. As the
286 result, an effective center of dipole locates at the depth of 43 R_p. While the remanence
287 intensity at the SRM region is smaller than that of TRM, the volume of SRM region is
288 significantly larger than that of TRM, resulting in the large contribution to the magnetic

289 anomaly. This distinct feature of the anomaly expressed as the two dipoles located at the
290 basement of the crater and a deeper part could be used to detect the magnetic anomaly
291 caused by impact events and would play an important role in reconstructing the magnetic
292 field histories of terrestrial planets. However, a more systematic study based on impact
293 simulations under various conditions and these magnetic anomaly calculations are
294 required to further evaluate the detectability of impact magnetization events on terrestrial
295 planets.
296
297 **5. Conclusion**
298 This study conducted two series of SRM acquisition experiments varying
299 applied fields and projectile conditions and the remanence measurements for cube-shaped
300 subsamples were conducted for the cylindrical basalt samples containing SD
301 titanomagnetite. The normalized SRM intensity and SRM stability values were similar in
302 the experiments with varying applied fields, and the SRM intensity was proportional to
303 the apple field intensity up to 400 μT. The SRM intensities for different projectile
304 conditions were almost consistent at the same P_{peak} values. Then, the empirical expression

for SRM intensity is proposed to be the power function of P_{peak} and a linear function of T_{peak}, which can be used to express the experimental SRM intensity values in the ranges P_{peak} up to 10 GPa and T_{peak} up to the Curie temperature. This empirical equation can be used to estimate the magnetic anomaly distribution over an impact crater. The anomaly showed a distinct feature approximated as two dipoles located at the basement of the crater and a deeper part, and this feature could be used to detect the magnetic anomaly caused by impact events.

Data Availability Statement

Data from this paper are archived at the UTokyo Repository (Sato, 2023). The iSALE shock physics code is not fully open-source, but is distributed on a case-by-case basis to academic users in the impact community for non-commercial use. A description of the application requirements can be found at the iSALE website (https://isale-code.github.io/terms-of-use.html). The M-ANEOS package is available from Thompson et al. (2019). The list of input parameters for the iSALE computations can be found in the Supplementary Information.

Acknowledgement

This study was performed under the collaborative research program with the Hypervelocity Impact Facility (former name: Space Plasma Laboratory), ISAS, JAXA. The authors thank the developers of iSALE, including G. Collins, K. Wünnemann, B. Ivanov, J. Melosh, and D. Elbeshausen. We used pySALEplot to analyze the output file of iSALE, and also thank Tom Davison for the development of pySALEPlot. This study was supported by JSPS KAKENHI grants JP21H01140. K.K. is supported by JSPS KAKENHI grant JP18KK0092 and JP19H00726. K.K. and M.S. are supported by JSPS KAKENHI grant JP21K18660.

References

1. Acuña, M. H., Connerney, J. E. P., Lin, R. P., Mitchell, D., Carlson, C. W., McFadden, J., et al. (1999). Global distribution of crustal magnetization discovered by the Mars Global Surveyor MAG/ER experiment. Science, 284(5415), 790–793.

2. Amsden, A., Ruppel, H., and Hirt, C. (1980). SALE: A simplified ALE computer

337 program for fluid flow at all speeds, Los Alamos National Laboratories Report, LA-
338 8095:101p.
339 3. Dunlop, D. J., & Özdemir, Ö. (1997). Rock magnetism: Fundamentals and frontiers,
340 (p. 573). Cambridge University Press.
341 4. Gattacceca, J., L. Berthe, M. Boustie, F. Vadeboin, P. Rochette, and T. De Resseguier
342 (2008), On the efficiency of shock magnetization processes, Phys. Earth Planet.
343 Inter., 166, 1–10.
344 5. Gattacceca, J., M. Boustie, E. Lima, B. P. Weiss, T. de Resseguier, and J.-P. Cuq-
345 Lelandais (2010), Unraveling the simultaneous shock magnetization and
346 demagnetization of rocks, Phys. Earth Planet. Inter., 182, 42–49.
347 6. Halekas, J. S., R. P. Lin, and D. L. Mitchell (2003), Magnetic fields of lunar multi-
348 ring impact basins, Meteorit. Planet. Sci., 38, 565–578.
349 7. Hood, L. L. (2011), Central magnetic anomalies of Nectarian-aged lunar impact
350 basins: Probable evidence for an early core dynamo, Icarus, 211, 1109–1128.
351 8. Ivanov, B. A., Deniem, D., and Neukum, G. (1997). Implementation of dynamic
352 strength models into 2-D hydrocodes: Applications for atmospheric breakup and

353 impact cratering. International Journal of Impact Engineering, 20(1–5), 411–430.

354 9. Kawai, N., K. Tsurui, S. Hasegawa, and E. Sato (2010), Single microparticle
355 launching method using two-stage light-gas gun for simulating hypervelocity
356 impacts of micrometeoroids and space debris, Rev. Sci. Instrum., 81, 115105.

357 10. Lillis, R. J., Robbins, S., Manga, M., Halekas, J. S., & Frey, H. V. (2013). Time
358 history of the Martian dynamo from crater magnetic field analysis. Journal of
359 Geophysical Research: Planets, 118, 1488–1511.

360 11. Néel, L. (1949), Théorie du traînage magnétique des ferromagnétiques en grains fins
361 avec applications aux terres cuites, Ann. Geophys., 5, 99–136.

362 12. Quesnel, Y., J. Gattacceca, G. R. Osinski, and P. Rochette (2013), Origin of the
363 central magnetic anomaly at the Haughton impact structure, Canada, Earth Planet.
364 Sci. Lett., 367, 116–122.

365 13. Sato, M. (2023). Data in “Pressure and temperature dependence of shock remanence
366 intensity for single-domain titanomagnetite-bearing basalt: Toward understanding
367 the magnetic anomalies produced by impact events”. Retrieved from
368 http://hdl.handle.net/2261/0002006019.

14. Sato, M., Kurosawa, K., Kato, S., Ushioda, M., & Hasegawa, S. (2021), Shock remanent magnetization intensity and stability distributions of single-domain titanomagnetite-bearing basalt sample under the pressure range of 0.1–10 GPa. Geophysical Research Letters, 48, e2021GL092716.

15. Sato, M., S. Yamamoto, Y. Yamamoto, Y. Okada, M. Ohno, H. Tsunakawa, and S. Maruyama (2015), Rock-magnetic properties of single zircon crystals sampled from the Tanzawa tonalitic pluton, central Japan, Earth Planets Space, 67, 150.

16. Srnka, L., G. Martelli, G. Newton, S. Cisowski, M. Fuller, and R. Schaal (1979), Magnetic field and shock effects and remanent magnetization in a hypervelocity impact experiment, Earth Planet. Sci. Lett., 42, 127–137.

17. Wünnemann, K., Collins, G. S., and Melosh, H. J. (2006). A strain-based porosity model for use in hydrocode simulations of impacts and implications for transient crater growth in porous targets. Icarus, 180(2), 514–527.

Figure 1. Orthogonal vector plots for stepwise alternating field demagnetization of shock remanence (cylindrical basalt sample 3767). Closed and open symbols denote projections

385 for X–Y and X–Z planes, respectively.

386

387 **Figure 2.** Shock remanence intensity plotted as a function of distance from the impact

388 point (cylindrical basalt samples 3767 and 3769).

389

390 **Figure 3.** Stepwise alternating field demagnetization curves for shock remanences

391 (cylindrical basalt sample 3767). Normalized remanence intensity is plotted as a function

392 of peak alternating field.

393

394 **Figure 4.** Shock remanence intensity plotted as a function of peak pressure during the

395 shock wave propagation. Closed and open black circles denote the data of this study

396 (cylindrical basalt sample 3767) within and beyond 3 cm from impact point, respectively.

397 Grey circles denote the data in Sato et al. (2021).

398

399 **Figure 5.** Orthogonal vector plots for stepwise thermal demagnetization of shock

400 remanence (cylindrical basalt sample 835). Closed and open symbols denote projections

401 for X–Y and X–Z planes, respectively.

402

403 **Figure 6.** Stepwise thermal demagnetization curves for shock remanences (cylindrical
404 basalt sample 835). Normalized remanence intensity is plotted as a function of peak
405 heating temperature.

406

407 **Figure 7.** Shock remanence (SRM) intensity (a) and stability (b) are plotted as a function
408 of peak pressure during the shock wave propagation for the cylindrical basalt samples
409 835, 838, 839, and 840. The SRM intensity was calculated as $(J_{SRM}/B_{SRM})/(J_{ARM}/B_{ARM})$,
410 where the J_{SRM}, J_{ARM}, B_{SRM}, and B_{ARM} are the SRM intensity, anhysteretic remanence
411 intensity, applied field intensity in SRM experiment, and applied DC field intensity in
412 ARM experiment. The shock remanence stability was calculated as $|\boldsymbol{J}_{SRM}(6) - \boldsymbol{J}_{SRM}(80)|/|$
413 $\boldsymbol{J}_{SRM}(2) - \boldsymbol{J}_{SRM}(80)|$, where $\boldsymbol{J}_{SRM}(X)$ is the SRM vector at the X mT AFD step. SRM
414 intensity (c) and stability (d) are plotted as a function of peak pressure during the shock
415 wave propagation for the cylindrical basalt samples 835, 836, 837, 3767, and 3773. The
416 SRM intensity was calculated as J_{SRM}/J_{ARM}. Black and gray lines in (c) are the linear

417 regression and power function lines, respectively.

418

419 **Figure 8.** Shock remanent magnetization (SRM) intensity (a and c) and stability (b and
420 d) are plotted as a function of peak temperature during the shock wave propagation
421 (cylindrical basalt samples 835, 836, 837, 3767, and 3773). The SRM intensity was
422 calculated as $|\boldsymbol{J}_{SRM}(2) - \boldsymbol{J}_{SRM}(80)|/|\boldsymbol{J}_{ARM} - \boldsymbol{J}_{ARM}(80)|$, where the $\boldsymbol{J}_{SRM}$ and $\boldsymbol{J}_{ARM}$ are the
423 SRM and anhysteretic remanence vectors, respectively, and the numbers in parentheses
424 indicate peak amplitude of alternating field demagnetization treatments. The shock
425 remanence stability was calculated as $|\boldsymbol{J}_{SRM}(6) - \boldsymbol{J}_{SRM}(80)|/|\boldsymbol{J}_{SRM}(2) - \boldsymbol{J}_{SRM}(80)|$.

426

427 **Figure 9.** (a) Relationship between the experimental and model SRM intensities. (b)
428 Differences between the experimental and model SRM intensity. Sizes of symbols
429 indicate the magnitude of residual values.

430

431 **Figure 10.** (a) Amplitudes of crustal magnetic fields at an altitude of 20 projectile radius
432 (R_p). Two-dimensional maps for (b) crustal remanence intensity, (c) peak pressure during

433 the shock wave propagation, and (d) peak temperature during the shock wave propagation.

434 The remanence intensity of shock remanence (SRM) is normalized with respect to that of

435 thermal remanent magnetization (TRM). The vertical and radial distances in the two-

436 dimensional maps are normalized with respect to R_p.

Figure 1.

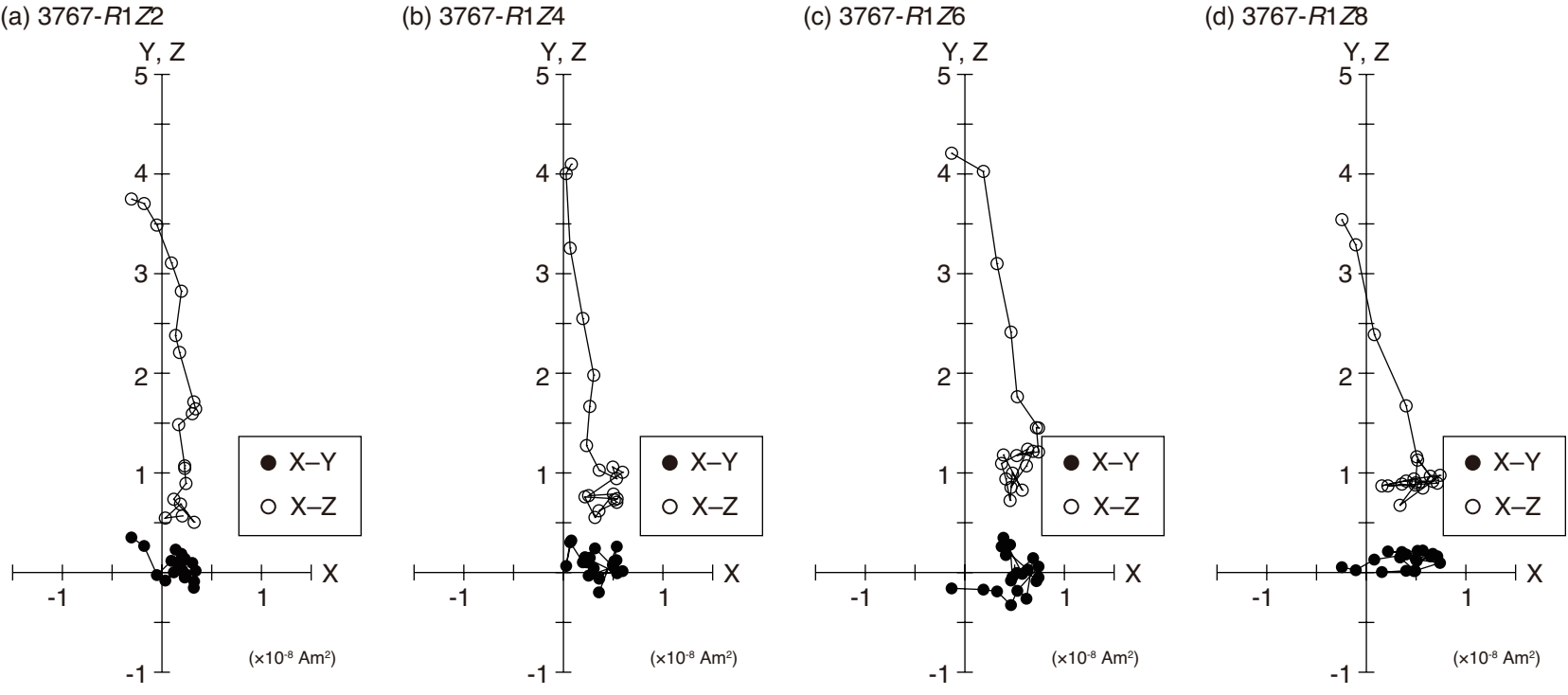
(a) 3767-R1Z2
(b) 3767-R1Z4
(c) 3767-R1Z6
(d) 3767-R1Z8
Y, Z
X
5
4
3
2
1
-1
X–Y
X–Z
(×10-8 Am2)

Figure 2.

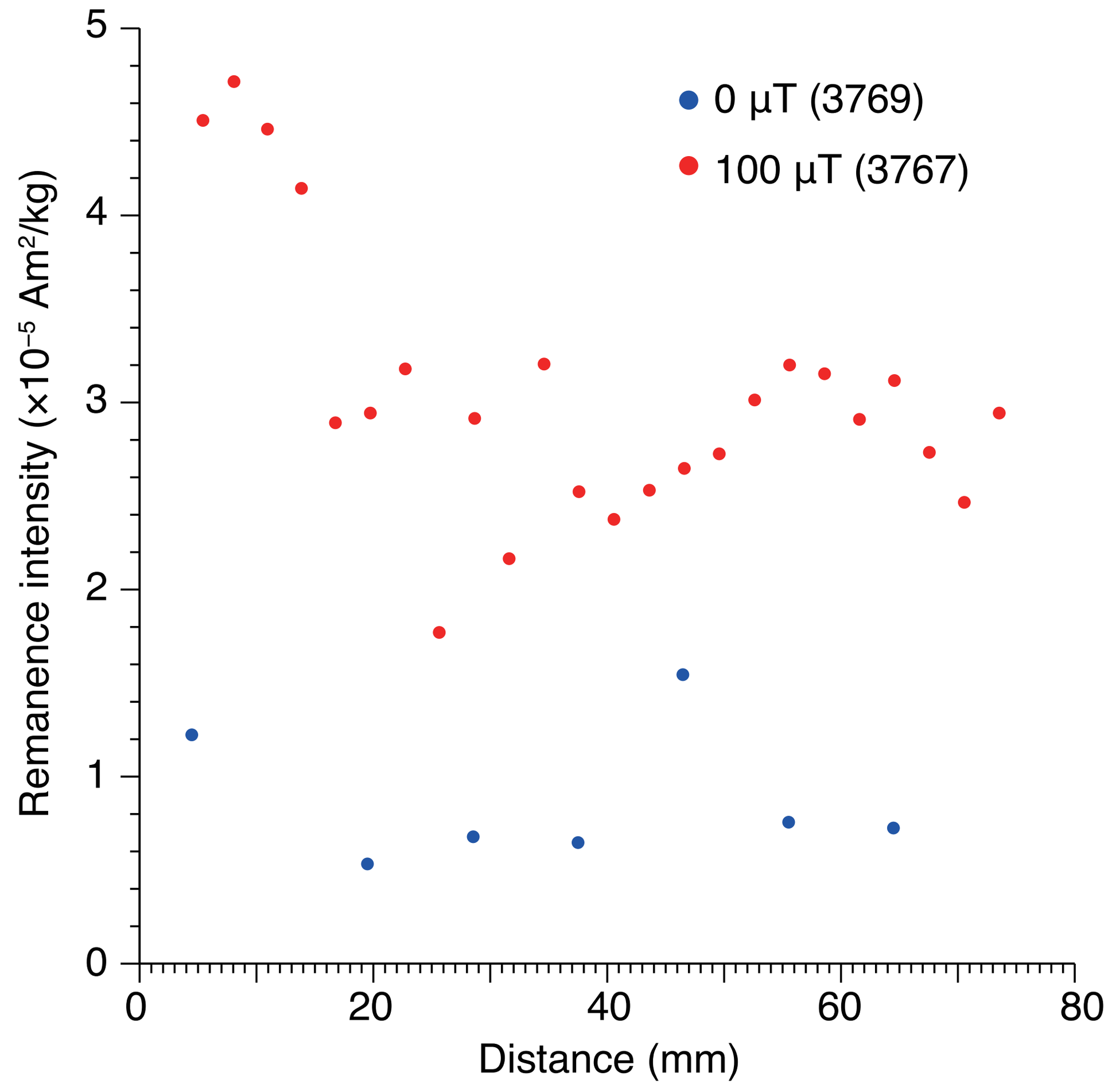
0 µT (3769)
100 µT (3767)
Remanence intensity (x10⁻⁵ Am²/kg)
Distance (mm)
0
1
2
3
4
5
0
20
40
60
80

Figure 3.

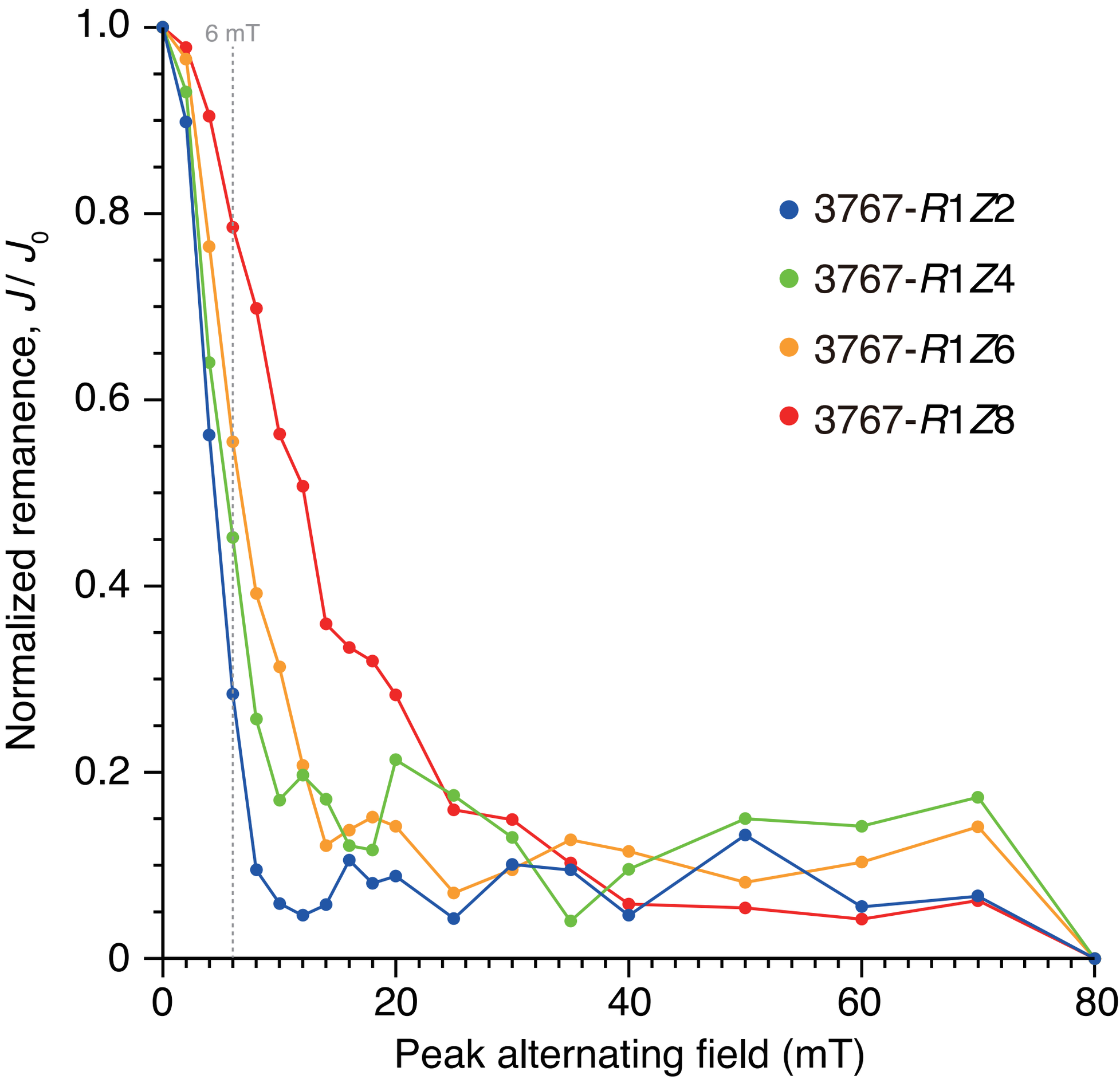
1.0
0.8
0.6
0.4
0.2
0
6 mT
Normalized remanence, J/ J0
0
20
40
60
80
Peak alternating field (mT)
3767-R1Z2
3767-R1Z4
3767-R1Z6
3767-R1Z8

Figure 4.

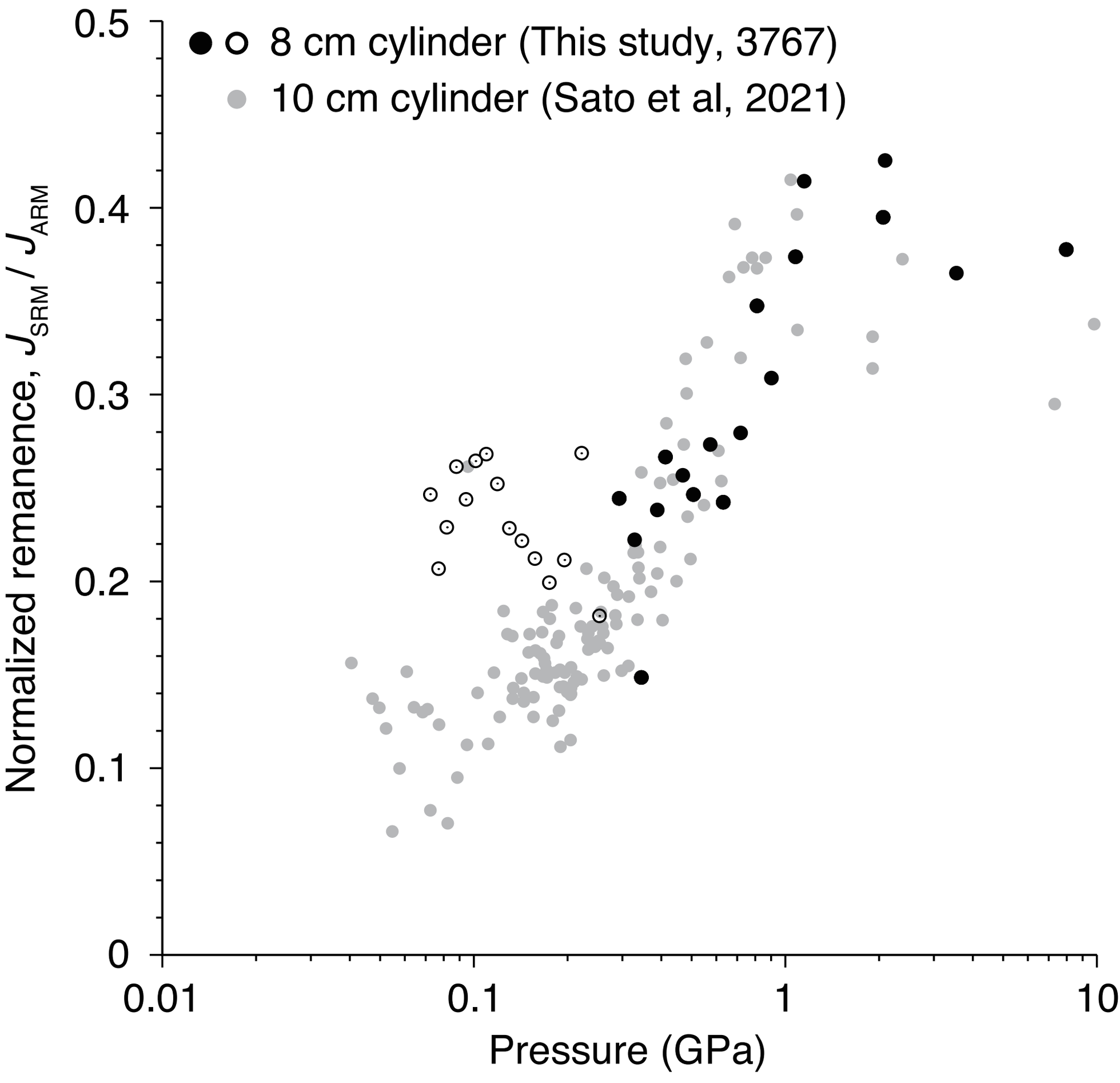
8 cm cylinder (This study, 3767)
10 cm cylinder (Sato et al, 2021)
Normalized remanence, J_{SRM} / J_{ARM}
0.5
0.4
0.3
0.2
0.1
0
0.01
0.1
1
10
Pressure (GPa)

Figure 5.

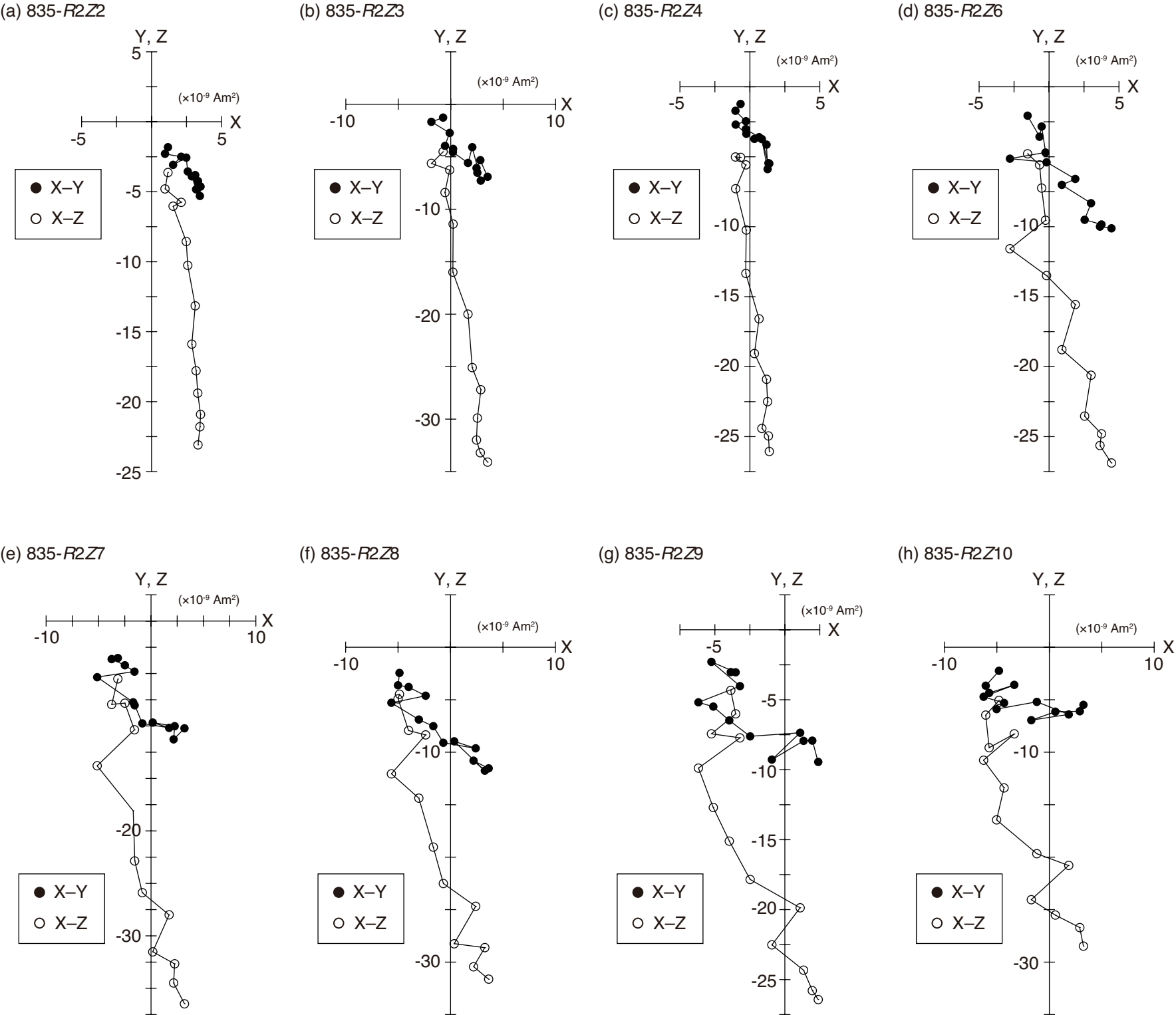
(a) 835-R2Z2
(b) 835-R2Z3
(c) 835-R2Z4
(d) 835-R2Z6
(e) 835-R2Z7
(f) 835-R2Z8
(g) 835-R2Z9
(h) 835-R2Z10
Y, Z
X
(×10⁻⁹ Am²)
X–Y
X–Z

Figure 6.

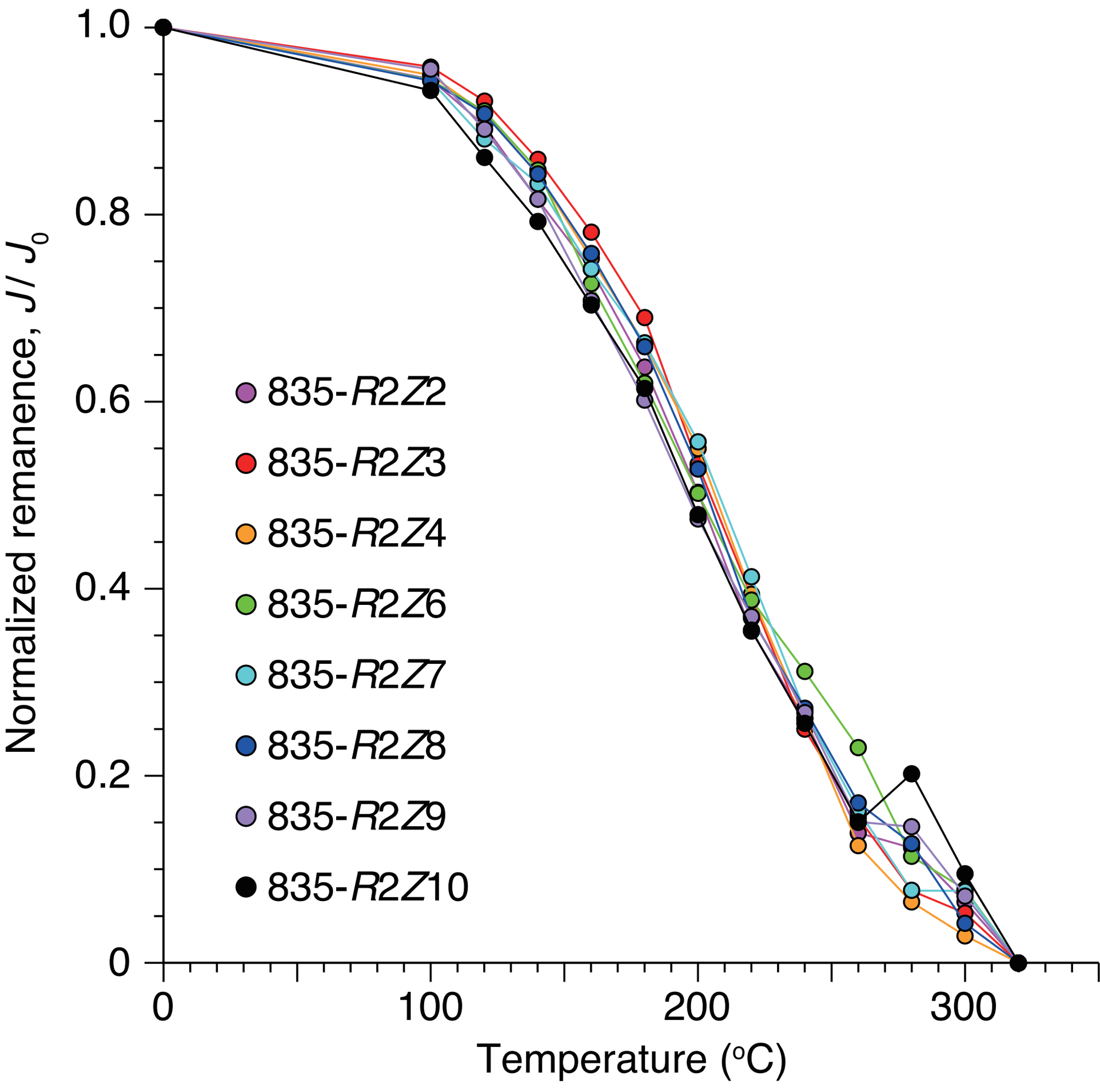
1.0
0.8
0.6
0.4
0.2
0
Normalized remanence, J/ J0
0
100
200
300
Temperature (°C)
835-R2Z2
835-R2Z3
835-R2Z4
835-R2Z6
835-R2Z7
835-R2Z8
835-R2Z9
835-R2Z10

Figure 7.

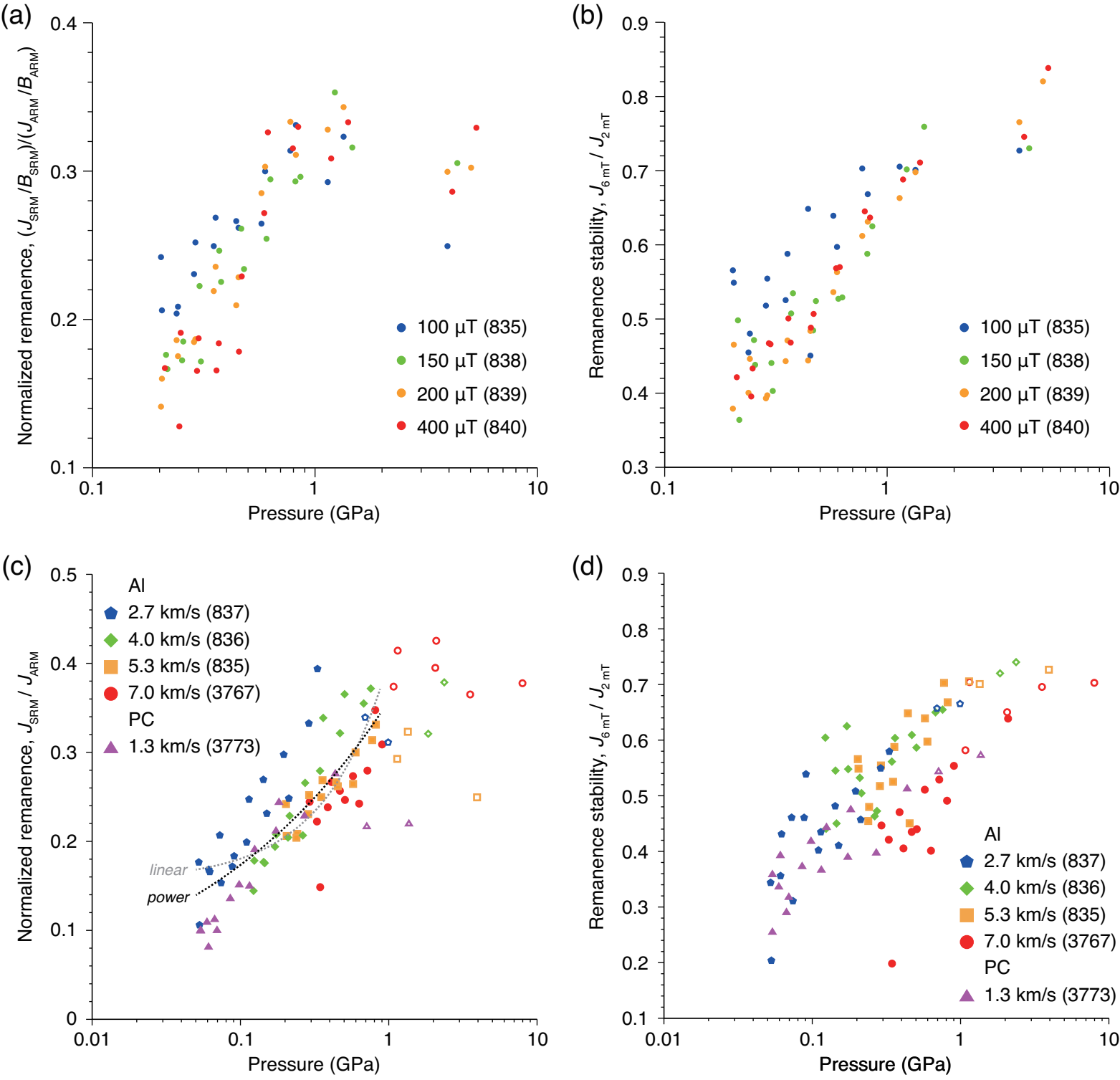
(a)
Normalized remanence, $(J_{SRM}/B_{SRM})/(J_{ARM}/B_{ARM})$
0.4
0.3
0.2
0.1
0.1
1
10
Pressure (GPa)
100 μT (835)
150 μT (838)
200 μT (839)
400 μT (840)
(b)
Remanence stability, $J_{6\,mT}/J_{2\,mT}$
0.9
0.8
0.7
0.6
0.5
0.4
0.3
0.1
1
10
Pressure (GPa)
100 μT (835)
150 μT (838)
200 μT (839)
400 μT (840)
(c)
Normalized remanence, J_{SRM}/J_{ARM}
0.5
0.4
0.3
0.2
0.1
0
0.01
0.1
1
10
Pressure (GPa)
Al
2.7 km/s (837)
4.0 km/s (836)
5.3 km/s (835)
7.0 km/s (3767)
PC
1.3 km/s (3773)
linear
power
(d)
Remanence stability, $J_{6\,mT}/J_{2\,mT}$
0.9
0.8
0.7
0.6
0.5
0.4
0.3
0.2
0.1
0.01
0.1
1
10
Pressure (GPa)
Al
2.7 km/s (837)
4.0 km/s (836)
5.3 km/s (835)
7.0 km/s (3767)
PC
1.3 km/s (3773)

Figure 8.

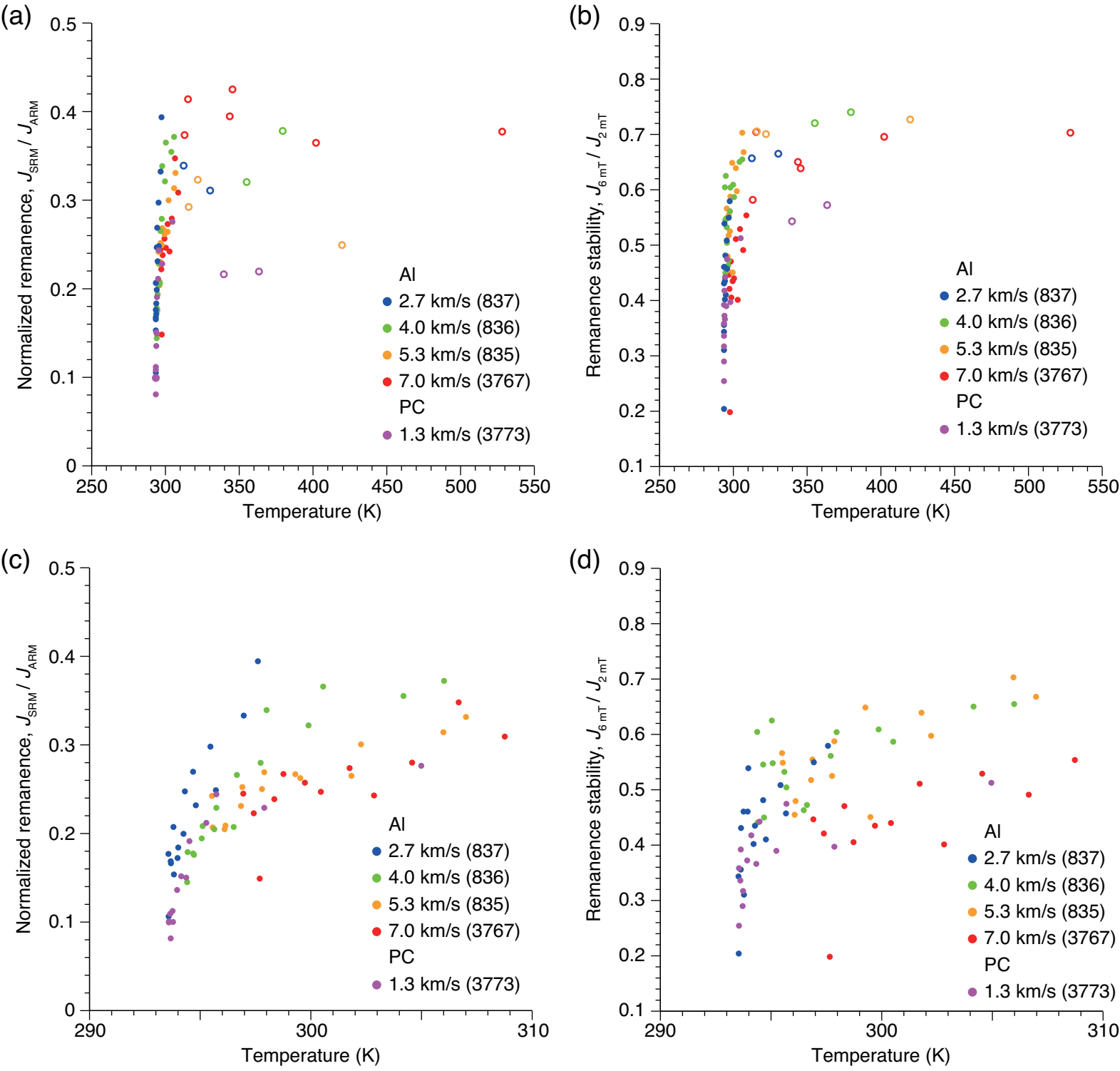
(a)
Normalized remanence, J_{SRM} / J_{ARM}
Temperature (K)
Al
2.7 km/s (837)
4.0 km/s (836)
5.3 km/s (835)
7.0 km/s (3767)
PC
1.3 km/s (3773)
(b)
Remanence stability, $J_{6\,mT}$ / $J_{2\,mT}$
Temperature (K)
Al
2.7 km/s (837)
4.0 km/s (836)
5.3 km/s (835)
7.0 km/s (3767)
PC
1.3 km/s (3773)
(c)
Normalized remanence, J_{SRM} / J_{ARM}
Temperature (K)
Al
2.7 km/s (837)
4.0 km/s (836)
5.3 km/s (835)
7.0 km/s (3767)
PC
1.3 km/s (3773)
(d)
Remanence stability, $J_{6\,mT}$ / $J_{2\,mT}$
Temperature (K)
Al
2.7 km/s (837)
4.0 km/s (836)
5.3 km/s (835)
7.0 km/s (3767)
PC
1.3 km/s (3773)

Figure 9.

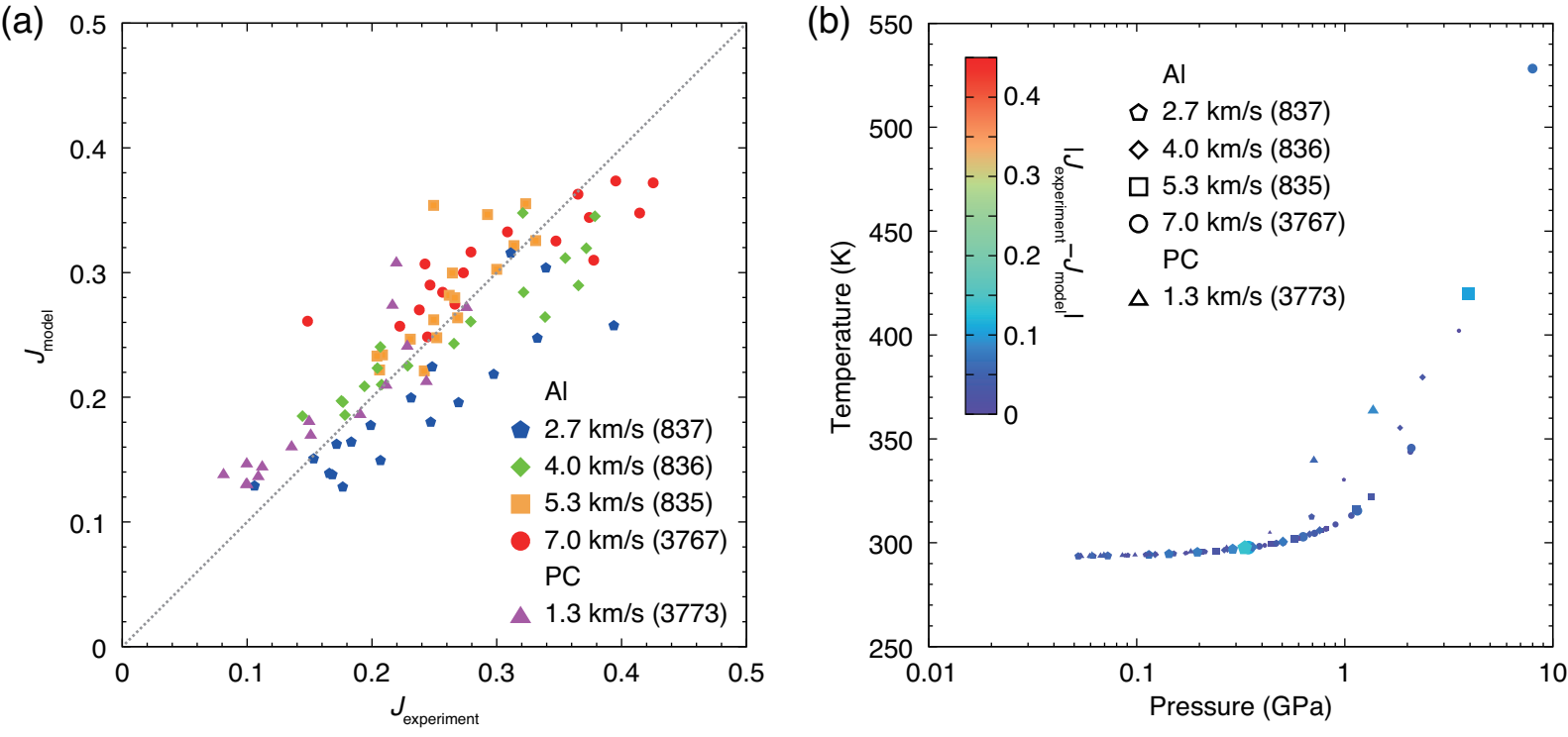
(a)
0.5
0.4
0.3
0.2
0.1
0
J_{model}
0
0.1
0.2
0.3
0.4
0.5
$J_{experiment}$
Al
2.7 km/s (837)
4.0 km/s (836)
5.3 km/s (835)
7.0 km/s (3767)
PC
1.3 km/s (3773)
(b)
550
500
450
400
350
300
250
Temperature (K)
0.01
0.1
1
10
Pressure (GPa)
0.4
0.3
0.2
0.1
0
$|J_{experiment} - J_{model}|$
Al
2.7 km/s (837)
4.0 km/s (836)
5.3 km/s (835)
7.0 km/s (3767)
PC
1.3 km/s (3773)

Figure 10.

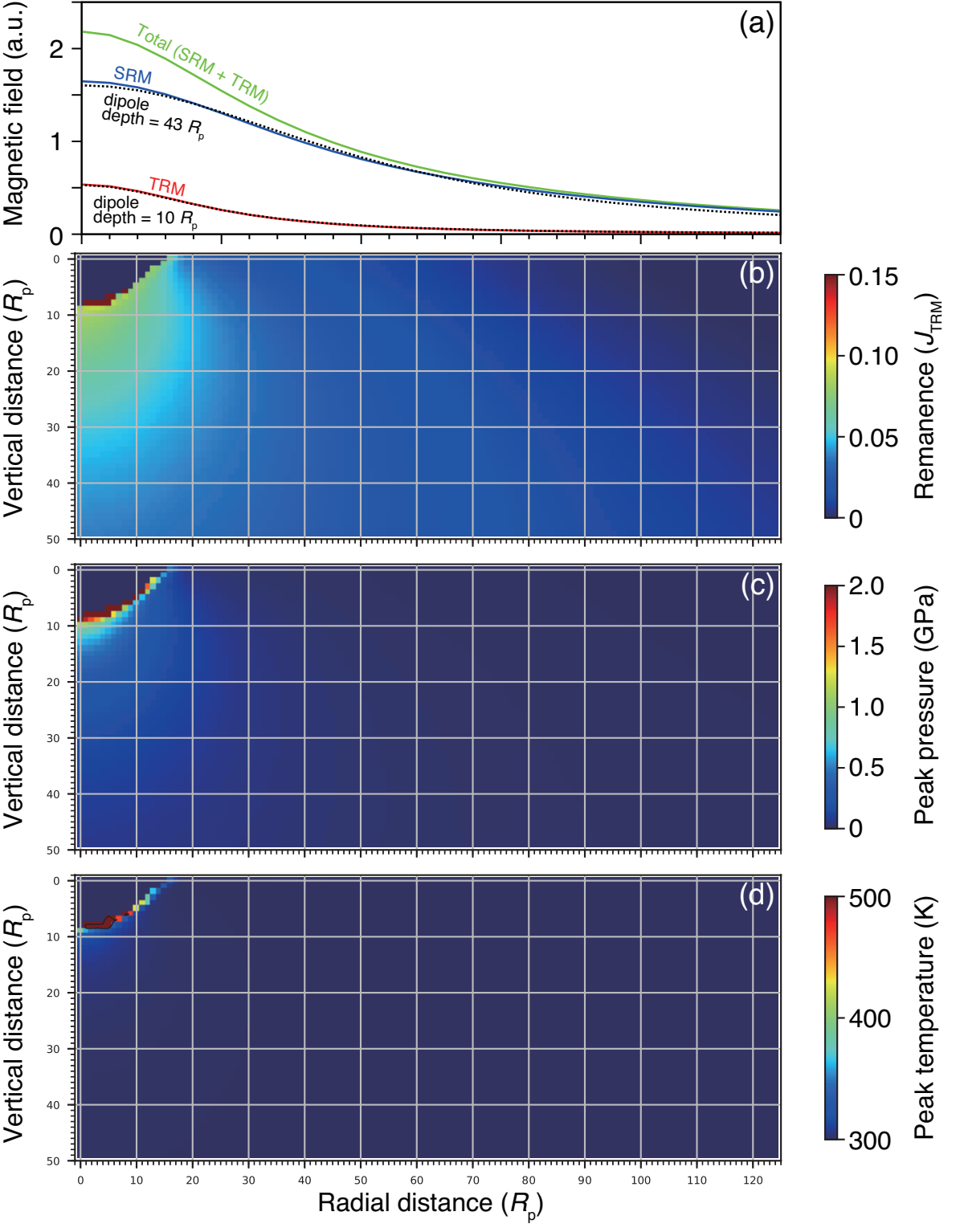
(a)
Magnetic field (a.u.)
Total (SRM + TRM)
SRM
dipole
depth = 43 R_p
TRM
dipole
depth = 10 R_p
(b)
Vertical distance (R_p)
Remanence (J_{TRM})
(c)
Peak pressure (GPa)
(d)
Peak temperature (K)
Radial distance (R_p)

Table 1. Summary of experimental samples

Cylinder ID	Gun-type	Projectile Material/Diameter	Impactor velocity (km/s)	Magnetic field (μT)
835	Vertical	Al 2 mm	5.3	100
836	Vertical	Al 2 mm	4.0	100
837	Vertical	Al 2 mm	2.7	100
838	Vertical	Al 2 mm	5.5	150
839	Vertical	Al 2 mm	5.3	200
840	Vertical	Al 2 mm	5.4	400
3767	Horizontal	Al 2 mm	7.0	100
3769	Horizontal	Al 2 mm	7.0	0
3773	Horizontal	PC 7 mm	1.3	100

Table 2. Summary of shock remanence measurements

Cylinder ID	Cube ID		
	R	*Z*	Treatment
835	1	3–10	AFD at 2 and 80 mT
	2	2–10	AFD at 2 and 80 mT
	2	2–4 and 6–10	THD at 100–320 °C
836	1	2–10	AFD at 2 and 80 mT
	2	2–10	AFD at 2 and 80 mT
837	1	2–10	AFD at 2 and 80 mT
	2	2–10	AFD at 2 and 80 mT
838	1	3–10	AFD at 2 and 80 mT
	2	2–10	AFD at 2 and 80 mT
839	1	2–10	AFD at 2 and 80 mT
	2	2–10	AFD at 2 and 80 mT
840	1	2–10	AFD at 2 and 80 mT
	2	2–10	AFD at 2 and 80 mT
3767	1	2, 4, 6, and 8	AFD at 2–80 mT
	2	2–25	AFD at 2 and 80 mT
	3	1–9	AFD at 2 and 80 mT
3769	1	1, 6, 9, 12, 15, 18, and 21	AFD at 2 and 80 mT
3773	2	1–6, 8, and 9	AFD at 2 and 80 mT
	3	1–9	AFD at 2 and 80 mT

AFD: alternating field demagnetization.